International Journal of Material Forming (2022) 15: 38
https://doi.org/10.1007/s12289-022-01673-9

ORIGINAL RESEARCH

Comparative study of various hardening models for the prediction of plastic responses under strain path change conditions

Wen Zhang[1] · Huachao Yang[1] · Xincun Zhuang[1] · Hongfei Wu[1] · Zhen Zhao[1,2]

Received: 7 October 2021 / Accepted: 23 February 2022 / Published online: 13 April 2022

Abstract

This work is aimed at investigating the influence of hardening models on the prediction of plastic responses of sheet metals under strain path change conditions. An enhanced back-stress restoration evolution hardening model was proposed, considering that the back stress accumulated in preloading stages was restored gradually in the subsequent loading stage. A comparative study was conducted between the proposed model and other two hardening models, i.e. Chaboche combined hardening model and Yoshida-Uemori hardening model, in terms of their prediction accuracy of work-hardening and r-value evolution behaviors under reverse and orthogonal loading conditions. The parameters in the models were determined by the experimental results of uniaxial tension and uniaxial compression-tension-compression tests using 6061O aluminum sheet. Associated with the Yld2000-2d yield function, these three hardening models were further employed to simulate a two-stage deep drawing process of a cylindrical cup. The predicted punch load-stroke curves, the height distribution of the drawn cup, and the split-ring springback were compared with the experimental ones. Obvious difference between the predictions was observed in the second drawing stage, which indicates the significant influence of hardening model on the prediction of plastic response under strain path change conditions. Among these three hardening models, the proposed hardening model presented a good prediction result which matched well with the experimental outcome.

Keywords Strain path change · Hardening model · Stress-strain relation · R-value · Sheet metal forming

Introduction

During the process of sheet metal forming, especially the multi-stage sheet metal forming, material can experience a variable-path loading condition that leads to complex strain path change. The stress and strain responses under strain path change are different from those under monotonic strain path [1, 2]. For example, in reverse loading the work-hardening characteristics including the Bauschinger effect, work-hardening stagnation, and permanent softening are usually observed, and in orthogonal loading the downward transition behavior of r-value is found besides the work-hardening behavior [3, 4].

Accuracy of numerical simulation of sheet metal forming process relies on an appropriate description of material behavior. Numerous studies are focused on the elastoplastic constitutive equations that are applicable to variable-path loading cases, containing anisotropic yield criterion, hardening law, and plastic flow rule. The hardening model is highlighted because it controls the evolution of yield surface during deformation, which is crucial to describe the stress and strain responses. Various hardening models including isotropic, kinematic, and mixed hardening have been proposed.

To capture the Bauschinger effect in reverse loading, linear kinematic hardening model [5] and nonlinear kinematic hardening model [6] are proposed by defining a back stress which denotes the position of yield surface. In these models, the yield surface translates according to the evolution of back stress without expansion. Later Chaboche [7] proposed a mixed isotropic–kinematic hardening model, allowing

✉ Xincun Zhuang
georgezxc@sjtu.edu.cn

✉ Zhen Zhao
zzhao@sjtu.edu.cn

1 Institute of Forming Technology and Equipment, School of Materials Science and Engineering, Shanghai Jiao Tong University, 200030 Shanghai, China

2 National Engineering Research Center of Die & Mold CAD, Shanghai Jiao Tong University, 200030 Shanghai, China

both the expansion and translation of yield surface. The model is widely used in predicting the material behavior under strain path change conditions, and has been embedded in many commercial finite element software. However, the Chaboche model is not capable of capturing the work-hardening stagnation that appears in the reverse loading for some material such as mild steel. To overcome that, Yoshida and Uemori [8] proposed a two-surface model by assuming the kinematic hardening of the yield surface within the bounding surface of mixed isotropic–kinematic hardening. The Yoshida-Uemori (YU) model and its derivatives have been recommended for predicting the deformation behavior and springback in sheet stamping process [9, 10]. Zhang et al. [11] proposed a mixed hardening model which consists of a restoration evolution rule of back stress and isotropic hardening for two-stage loading experiments. The model is characterized by describing the isotropic expansion of yield surface for the as-received sheet and the anisotropic expansion of yield surface for the prestrained sheet. The abovementioned models define the evolution of back stress, which controls the translation of yield surface, to capture the work-hardening behavior in strain path change conditions. However, their ability to describe the downward transition of r-value is rarely reported.

Barlat et al. [12] proposed a homogeneous anisotropic hardening (HAH) model, which does not refer to the concept of back stress. The HAH model defines a stable component to describe the isotropic expansion of yield surface and a fluctuation component to describe the distortion of the yield surface. The model and its derivatives can capture the Bauschinger effect, work-hardening stagnation, and permanent softening [13, 14] in variable loading cases. Qin et al. [15] and Zaman et al. [16] utilized the HAH model to predict the r-value transition of aluminum and advanced high-strength steel sheets under strain path change conditions, and the results were reasonable. The complicated mathematical formula of the HAH model enables the good description ability for the stress and strain response, but also restricts its application in the practical forming processes.

In this work, an enhanced back-stress restoration evolution (enhanced-BRE) hardening model for arbitrary strain path change conditions was proposed, and the prediction ability in terms of describing stress and strain response was compared with that of Chaboche combined hardening model and YU hardening model. Theoretical formula of these three hardening models, associated with the Yld2000-2d yield function, are introduced in Sect. 2. Uniaxial tension and uniaxial compression-tension-compression tests using 6061O aluminum sheet were utilized to determine the parameters in the abovementioned models. The experiment method, parameter identification process, and the stress and r-value results predicted by the identified models are shown in Sect. 3. Section 4 presents the detailied comparative study of applying these three hardening models in a two-stage deep drawing process.

Theoretical formula

Yld2000-2d yield function

A non-quadratic yield function proposed by Barlat et al. [17], i.e. the so-called Yld2000-2d yield function, is utilized here to describe the anisotropy of metallic sheet. The Yld2000-2d function can be written as:

$$f = \phi(\eta) - 2(\sigma_{y0} + R)^m = \phi' + \phi'' - 2(\sigma_{y0} + R)^m = 0 \quad (1)$$

where the stress tensor $\boldsymbol{\eta}$ is defined as $\boldsymbol{\eta} = \boldsymbol{\sigma} - \boldsymbol{\alpha}$; $\boldsymbol{\sigma}$ is the Cauchy stress tensor; $\boldsymbol{\alpha}$ is the back stress tensor; σ_{y0} is the yield stress along the reference direction of the sheet; R is isotropic hardening component of yield surface; the exponent m is recommended as $m = 8$ for face-centered cubic (FCC) metals and $m = 6$ for body-centered cubic (BCC) metals; and

$$\phi' = |X'_1 - X'_2|^m \quad (2a)$$

$$\phi'' = |X''_1 + 2X''_2|^m + |2X''_1 + X''_2|^m \quad (2b)$$

where $X_j^{'}$ and $X_j^{''}$ ($j = 1, 2$) are the principle values of $\mathbf{X}'$ and $\mathbf{X}''$ which are two linearly transformed stress tensor of $\boldsymbol{\eta}$. The linear transformations can be expressed as:

$$\mathbf{X}' = \mathbf{L}'.\eta \quad (3a)$$

$$\mathbf{X}'' = \mathbf{L}''.\eta \quad (3b)$$

where $\mathbf{L}'$ and $\mathbf{L}''$ are the coefficient matrixes of the linear transformation.

The abovementioned linear transformations can be rewritten in matrix notation as:

$$\begin{bmatrix} X'_{11} \\ X'_{22} \\ X'_{12} \end{bmatrix} = \begin{bmatrix} L'_{11} & L'_{12} & 0 \\ L'_{21} & L'_{22} & 0 \\ 0 & 0 & L'_{66} \end{bmatrix} \begin{bmatrix} \eta_{11} \\ \eta_{22} \\ \eta_{12} \end{bmatrix} \quad (4a)$$

$$\begin{bmatrix} X''_{11} \\ X''_{22} \\ X''_{12} \end{bmatrix} = \begin{bmatrix} L''_{11} & L''_{12} & 0 \\ L''_{21} & L''_{22} & 0 \\ 0 & 0 & L''_{66} \end{bmatrix} \begin{bmatrix} \eta_{11} \\ \eta_{22} \\ \eta_{12} \end{bmatrix} \quad (4b)$$

The principle values of $\mathbf{X}'$ and $\mathbf{X}''$ are:

$$\left.\begin{aligned} X'_1 &= \frac{1}{2}\left(X'_{11} + X'_{22} + \left((X'_{11} - X'_{22})^2 + 4X'^2_{12}\right)^{1/2}\right) \\ X'_2 &= \frac{1}{2}\left(X'_{11} + X'_{22} - \left((X'_{11} - X'_{22})^2 + 4X'^2_{12}\right)^{1/2}\right) \end{aligned}\right\} \tag{5a}$$

$$\left.\begin{aligned} X''_1 &= \frac{1}{2}\left(X''_{11} + X''_{22} + \left((X''_{11} - X''_{22})^2 + 4X''^2_{12}\right)^{1/2}\right) \\ X''_2 &= \frac{1}{2}\left(X''_{11} + X''_{22} - \left((X''_{11} - X''_{22})^2 + 4X''^2_{12}\right)^{1/2}\right) \end{aligned}\right\} \tag{5b}$$

The two coefficient matrixes of the linear transformation **L***'* and **L***''* can be expressed as follows.

$$\begin{bmatrix} L'_{11} \\ L'_{12} \\ L'_{21} \\ L'_{22} \\ L'_{66} \end{bmatrix} = \frac{1}{3}\begin{bmatrix} 2 & 0 & 0 \\ -1 & 0 & 0 \\ 0 & -1 & 0 \\ 0 & 2 & 0 \\ 0 & 0 & 1 \end{bmatrix}\begin{bmatrix} a_1 \\ a_2 \\ a_7 \end{bmatrix} \tag{6a}$$

$$\begin{bmatrix} L''_{11} \\ L''_{12} \\ L''_{21} \\ L''_{22} \\ L''_{66} \end{bmatrix} = \frac{1}{9}\begin{bmatrix} -2 & 2 & 8 & -2 & 0 \\ 1 & -4 & -4 & 4 & 0 \\ 4 & -4 & -4 & 1 & 0 \\ -2 & 8 & 2 & -2 & 0 \\ 0 & 0 & 0 & 0 & 9 \end{bmatrix}\begin{bmatrix} a_3 \\ a_4 \\ a_5 \\ a_6 \\ a_8 \end{bmatrix} \tag{6b}$$

where a_k ($k = 1 \sim 8$) are the independent parameters related to the anisotropy of sheet metals. If all the parameters a_k equal to 1, the yield function defined in Eq. (1) reduces to the isotropic expression.

Based on the assumption of associated flow rule, the plastic strain increment can be calculated by:

$$\mathrm{d}\varepsilon^{\mathrm{p}} = \mathrm{d}\lambda\frac{\partial\phi}{\partial\eta} = \mathrm{d}\lambda\left(\frac{\partial\phi'}{\partial\mathbf{X}'}\cdot\frac{\partial\mathbf{X}'}{\partial\eta} + \frac{\partial\phi''}{\partial\mathbf{X}''}\cdot\frac{\partial\mathbf{X}''}{\partial\eta}\right) = \mathrm{d}\lambda\left(\frac{\partial\phi'}{\partial\mathbf{X}'}\cdot\mathbf{L}' + \frac{\partial\phi''}{\partial\mathbf{X}''}\cdot\mathbf{L}''\right) \tag{7}$$

where $\mathrm{d}\boldsymbol{\varepsilon}^{\mathrm{p}}$ is the plastic strain increment; $\mathrm{d}\lambda$ is the plastic multiplier. Detailed expressions of Eq. (7) could be seen in the work of Barlat et al. [17],.

Hardening model

The hardening model defines the evolution of yield surface which is important to the prediction of stress and strain responses. Three kinds of hardening models, i.e. Chaboche combined hardening model (Chaboche model), enhanced back-stress restoration evolution hardening model (enhanced-BRE model), and Yoshida-Uemori hardening model (YU model), were utilized in this work. Detailed formulations are presented as bellow.

Chaboche combined hardening model

The hardening model proposed by Chaboche [7] consists of a kinematic hardening item and an isotropic hardening item. The kinematic hardening is defined as the evolution rule of back stress $\boldsymbol{\alpha}$, which controls the position of yield surface. By using multiple back stress components $\boldsymbol{\alpha}_{(i)}$ and assuming the Amstrong-Frederick rule (AF rule), the kinematic hardening can be expressed as:

$$\alpha = \sum_{i=1}^{n} \alpha_{(i)} \tag{8}$$

$$\mathrm{d}\alpha_{(i)} = \frac{2}{3}C_i\mathrm{d}\varepsilon^{\mathrm{p}} - \gamma_i\alpha_{(i)}\mathrm{d}p \tag{9}$$

where $\mathrm{d}p$ is the equivalent plastic strain increment; C_i and γ_i are material constants; C_i/γ_i determines the saturation value of back stress $\boldsymbol{\alpha}_{(i)}$, and γ_i controls the rate of saturation; n is the number of back stress components. The use of multiple back stress components in the Chaboche model can improve the prediction accuracy comparing with the classical Armstrong-Frederick model with only one back stress component. However, it is not appropriate to use as many back stress components as possible; on the contrary, this will increase the uncertainty of parameter identification. The use of two to four back stress components is acceptable in the relevant studies [18–20]. In this work, the Chaboche combined hardening model with three back stress components ($n = 3$) was employed due to the parameter identification method adopted in the following Sect. 3.2.2.

The isotropic hardening, defining the expansion of yield surface, is written as:

$$R = Q_1\left[1 - \exp\left(-b_1\bar{\varepsilon}^{\mathrm{p}}\right)\right] + Q_2\left[1 - \exp\left(-b_2\bar{\varepsilon}^{\mathrm{p}}\right)\right] \tag{10}$$

where $\bar{\varepsilon}^{\mathrm{p}}$ is the equivalent plastic strain; Q_1, b_1, Q_2, and b_2 are material constants.

Enhanced back-stress restoration evolution hardening model

Under the assumption that the back stress geometrically stands for the center from the uniaxial tension stress to the uniaxial compression stress on the yield surface, a restoration evolution of back stress was observed during two-stage loading tests by Zhang et al. [11]. To extend the back-stress restoration evolution hardening model (BRE model) to arbitrary strain path change conditions which usually exist in practical forming processes, the concepts of accumulated back stress and active back stress were introduced in this work.

The appearance of back stress is related to the microscale uniformity of plastic deformation. Therefore, the back stress should accumulate continuously throughout the deformation process. However, after the loading path changes, the back stress actually acting in the subsequent loading stage evolves under a combined influence of preloading and subsequent loading stages, and thus might show the characteristics of discontinuity. The continuously accumulated back stress against plastic deformation is called the accumulated back stress $\boldsymbol{\alpha}_a$, and the back stress that actually works in the yield function is called the active back stress (also simply called back stress, $\boldsymbol{\alpha}$). The enhanced-BRE model assumes that in the subsequent loading stage the active back stress gradually restores from the accumulated back stress at the end of preloading stage. The back stress that can be obtained from experiments is the active back stress.

The evolution of accumulated back stress $\boldsymbol{\alpha}_a$ is defined by the AF rule:

$$\mathrm{d}\alpha_{\mathrm{a}} = \frac{2}{3}C\mathrm{d}\varepsilon^{\mathrm{p}} - \gamma\alpha_{\mathrm{a}}\mathrm{d}p \tag{11}$$

The active back stress $\boldsymbol{\alpha}$ consists of the part reflecting the contribution of preloading $\boldsymbol{\alpha}_{pre}$, and the other part representing the restoration evolution mode of $\boldsymbol{\alpha}$ in the subsequent loading k_n:

$$\left.\begin{matrix}\alpha_{\mathrm{pre}} = \alpha_{\mathrm{a}} \\ \varepsilon^{\mathrm{p}}_{\mathrm{pre}} = \varepsilon^{\mathrm{p}}\end{matrix}\right\}, \text{ once the loading path changes} \tag{12}$$

$$\alpha = \alpha_{\mathrm{pre}} \cdot k_{\mathrm{n}} \tag{13}$$

where $\varepsilon^{\mathrm{p}}_{\mathrm{pre}}$ is the plastic prestrain, which equals to the plastic strain at the moment of load path change; k_n is a scaler function of the equivalent plastic strain in the subsequent loading stage:

$$k_{\mathrm{n}} = p + (1-p)\exp\left(-q\left(\bar{\varepsilon}^{\mathrm{p}} - \bar{\varepsilon}^{\mathrm{p}}_{\mathrm{pre}}\right)\right) \tag{14}$$

where p and q are material constants. Equation (14) shows two characteristics of k_n: (1) k_n = 1 at the beginning of the subsequent loading stage, and (2) k_n decreases gradually as the subsequent loading stage progresses. According to the experimental investigation, the back stress restores partially from the value $\boldsymbol{\alpha}_{pre}$ which equals to the accumulative back stress at the beginning of the subsequent loading stage, but never recovers. This requires that the saturation of k_n is constrained to be larger than zero, i.e. $0<p<1$ for Eq. (14).

If the back stress has multiple components, Eqs. (11)-(14) can be rewritten as:

$$\mathrm{d}\alpha_{\mathrm{a}(i)} = \frac{2}{3}C_i\mathrm{d}\varepsilon^{\mathrm{p}} - \gamma_i\alpha_{\mathrm{a}(i)}\mathrm{d}p \tag{15}$$

$$\left.\begin{matrix}\alpha_{\mathrm{pre}(i)} = \alpha_{\mathrm{a}(i)} \\ \varepsilon^{\mathrm{p}}_{\mathrm{pre}} = \varepsilon^{\mathrm{p}}\end{matrix}\right\}, \text{ once the loading path changes} \tag{16}$$

$$\alpha_{(i)} = \alpha_{\mathrm{pre}(i)} \cdot k_{\mathrm{n}(i)} \tag{17}$$

$$k_{\mathrm{n}(i)} = p_i + (1-p_i)\exp\left(-q_i\left(\bar{\varepsilon}^{\mathrm{p}} - \bar{\varepsilon}^{\mathrm{p}}_{\mathrm{pre}}\right)\right) \tag{18}$$

$$\alpha = \sum_{i=1}^{n}\alpha_{(i)} \tag{19}$$

The scalar coefficient $k_{n(i)}$ denotes the change of each stress component $\boldsymbol{\alpha}_{(i)}$ in the loading stage after the strain path changes. According to the expression of $k_{n(i)}$ shown as Eqs. (17) and (18), the parameter p_i stands for the saturation value of change ratio, i.e. $\alpha_{(i)}/\alpha_{pre(i)}$, when the strain is large enough; the sign of the term (1- p_i) represents the increase or decrease trend of the change, and the parameter q_i reflects how fast the back stress component researches its saturation value. In the current version of enhanced-BRE model, the back stress components are not given clear physical meanings, but their evolution trends construct the evolution of the total back stress. To ensure that the back stress $\boldsymbol{\alpha}$ restores partially from $\boldsymbol{\alpha}_{pre}$ in the subsequent loading stage, a simple but effective restriction between the saturations C_i/γ_i and p_i was proposed as:

$$\sum_{i=1}^{n}\frac{C_i}{\gamma_i}\cdot p_i > 0 \tag{20}$$

If the changed strain path is maintained for a period of strain range, k_n gradually reduces with the increase of strain, resulting in the gradual decrease of back stress. If the strain path changes continuously, k_n is always equal to 1, and thus $\boldsymbol{\alpha} = \boldsymbol{\alpha}_{pre} = \boldsymbol{\alpha}_a$, which means that in this case the restoration evolution rule of back stress reduces to the AF rule. The change of strain path is important to the restoration evolution of back stress. The parameter cos(θ) proposed by Schmitt et al. [21] can be utilized to measure the strain path change according to a lot of research [22, 23].

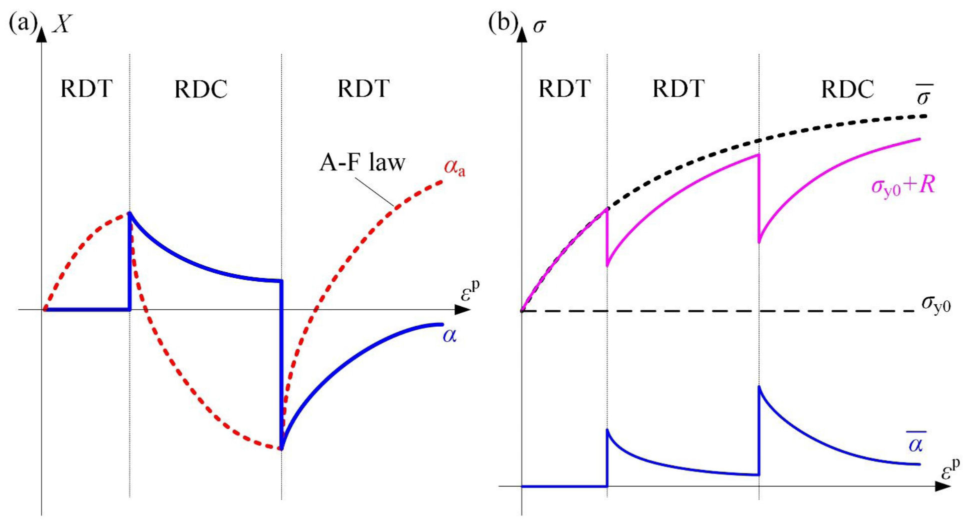

Fig. 1 Illustration of back stress evolution (a) and the relation of isotropic hardening rule and kinematic hardening rule (b) defined in the enhanced-BRE

$$\cos(\theta) = \frac{d\varepsilon_1^p : d\varepsilon_2^p}{\|d\varepsilon_1^p\| \cdot \|d\varepsilon_2^p\|} \tag{21}$$

where $d\varepsilon_1^p$ and $d\varepsilon_2^p$ are the plastic strain increments before and after current calculation step. When the strain path remains unchanged, $\cos(\theta) = 1$.

Figure 1a illustrates the evolution mode of back stress defined by the enhanced-BRE rule and AF rule in RD tension-compression tests. In the first loading stage, the back stress $\boldsymbol{\alpha}$ defined by the enhanced-BRE rule equals to zero; in each of the subsequent loading stages, the back stress gradually decreases but never reaches zero. By contrast, the back stress $\boldsymbol{\alpha}_a$ in the AF rule grows in the first loading stage; in the subsequent loading stages, the back stress decreases with the increase of strain firstly, and then increases inversely after $\boldsymbol{\alpha}_a$ decreases to zero.

Figure 1b illustrates the relation of isotropic hardening rule and kinematic hardening rule. For the sheet without prestrain, the flow curve in the reference direction can be described by the Voce + Voce model:

$$\bar{\sigma} = \sigma_{y0} + Q_1\left[1 - \exp\left(-b_1\bar{\varepsilon}^p\right)\right] + Q_2\left[1 - \exp\left(-b_2\bar{\varepsilon}^p\right)\right] \tag{22}$$

where Q_1, b_1, Q_2, and b_2 are material constants. For the sheet in variable-path loading cases, the isotropic hardening rule $R(\bar{\varepsilon}^p)$ can be defined as the difference between the flow stress ($\bar{\sigma}$) in the reference direction and the sum of the initial yield stress and equivalent back stress $\bar{\alpha}$:

$$R = \bar{\sigma} - (\sigma_{y0} + \bar{\alpha}) \tag{23}$$

Yoshida-Uemori hardening model

Yoshida and Uemori proposed a two-surface model for describing the deformation characteristics under large-strain cyclic loading conditions, especially the work-hardening stagnation. In the two-surface model, the yield surface moves kinematically within a bounding surface; only the kinematic hardening is assumed for the yield surface, while the mixed isotropic-kinematic hardening is defined for the bounding surface.

Associated with the Yld2000-2d yield function, the yield surface can be expressed as:

$$f = \phi(\sigma - \alpha) - 2\sigma_{y0}{}^m = 0 \tag{24}$$

The yield surface is utilized to calculate the plastic strain increment $d\boldsymbol{\varepsilon}^p$ under the assumption of associated flow rule shown as Eq. (8). The bounding surface is given by:

$$F = \phi(\sigma - \beta) - 2(B + R)^m = 0 \tag{25}$$

where the back stress $\boldsymbol{\beta}$ denotes the center of the bounding surface; B and R are the initial size and isotropic hardening component of the bounding surface.

The back stress $\boldsymbol{\alpha}$ of yield surface can be expressed by the sum:

$$\alpha = \alpha_* + \beta \tag{26}$$

where $\boldsymbol{\alpha}_*$ denotes the relative kinematic motion of the yield surface with respect to the bounding surface. The evolution of $\boldsymbol{\alpha}_*$ is defined based on a modification of AF rule:

$$d\alpha_* = Ca\left(\sqrt{\frac{2}{3}}d\varepsilon^p - \sqrt{\frac{\bar{\alpha}_*}{a}}\mathbf{n}_* dp\right) \tag{27}$$

where C is a material constant; $\bar{\alpha}_*$ is the equivalent value of $\boldsymbol{\alpha}_*$; $\mathbf{n}_*$ denote the unit tensor in the direction of $\boldsymbol{\alpha}_*$:

$$\mathbf{n}_* = \frac{\alpha_*}{\|\alpha_*\|} \tag{28}$$

The item a in Eq. (27) is expressed as:

$$a = B + R - \sigma_{y0} \tag{29}$$

The kinematic hardening of bounding surface is defined by the AF rule:

$$\mathrm{d}\beta = n\left(\frac{2}{3}b\mathrm{d}\varepsilon^{\mathrm{p}} - \beta\mathrm{d}p\right) \tag{30}$$

and its isotropic hardening is expressed as:

$$\mathrm{d}R = n\left(R_{\mathrm{sat}} - R\right)\mathrm{d}p \tag{31}$$

where n and b are material constants; R_{sat} is the saturated value of the isotropic hardening stress R at infinitely large plastic strain.

To describe the work-hardening stagnation, a mixed hardening surface g_σ is defined in the stress space.

$$g_\sigma = \phi(\sigma - \mathbf{q}) - 2r^m = 0 \tag{32}$$

where $\mathbf{q}$ and r are the center and size of the surface g_σ. It is assumed that the center of bounding surface $\boldsymbol{\beta}$ exists either on or inside of the surface g_σ. The isotropic hardening of the bounding surface R takes place only when $\boldsymbol{\beta}$ stays on the surface g_σ, namely

$$\begin{cases} \mathrm{d}R = m\left(R_{\mathrm{sat}} - R\right)\mathrm{d}p, \text{ if } \phi(\beta - \mathbf{q}) - 2r^m = 0 \text{ and } \frac{\partial\phi}{\partial\beta} : \mathrm{d}\beta > 0 \\ \mathrm{d}R = 0, \text{ otherwise} \end{cases} \tag{33}$$

The center of the surface g_σ is assumed to move in the direction of $(\boldsymbol{\beta} - \mathbf{q})$:

$$\mathrm{d}\mathbf{q} = \mu(\beta - \mathbf{q}) \tag{34}$$

By applying the consistency condition to Eq. (32) and considering Eq. (34), there is

$$\mu = \frac{\Gamma - \mathrm{d}r}{r} \text{ and } \Gamma = \frac{1}{2mr^{m-1}}\frac{\partial g_\sigma}{\partial(\beta - \mathbf{q})} : \mathrm{d}\beta \tag{35}$$

The evolution of isotropic hardening stress r is defined as:

$$\begin{cases} \mathrm{d}r = h\Gamma, \text{ when } \mathrm{d}R > 0 \\ \mathrm{d}r = 0, \text{ when } \mathrm{d}R = 0 \end{cases} \tag{36}$$

where h $(0 \le h \le 1)$ is a material constant that determines the rate of expansion of surface g_σ. The initial value of r is assumed to be zero in this work.

In summary, three kinds of hardening models, i.e. Chaboche model, enhanced-BRE model, and YU model, were utilized in this work. The ability of the models to describe the plastic response of sheet metals under variable-path loading conditions were investigated. Table 1 lists the parameters to be identified in these three models. Detailed identification process will be discussed later in Sect. 3.2.

Material experiments and parameter identification

To investigate the plastic response under variable-path loading conditions, 3 mm thick 6061O aluminum sheet was used

Table 1 Parameters to be identified in three kinds of hardening models

Hardening model	Parameters	
	Number	Symbols
Chaboche model	11	σ_{y0}, Q_1, b_1, Q_2, b_2, C_i, γ_i $(i=1,2,3)$
enhanced-BRE model	17	σ_{y0}, Q_1, b_1, Q_2, b_2, C_i, γ_i, p_i, q_i $(i=1,2,3)$
YU model	7	σ_{y0}, B, R_{sat}, n, C, b, h

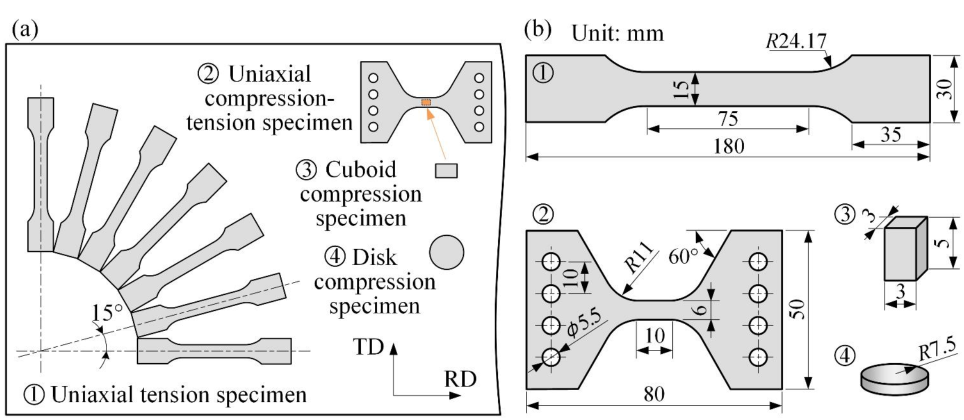

Fig. 2 Tension and compression experiments (a) testing method (b) dimensions of testing specimens

in this work. The in-plane uniaxial tension (UT), uniaxial compression-tension-compression (UCTC), and cuboid compression (CC) tests, as well as the though-thickness disk compression (DC) tests, were conducted to provide the stress-strain curves and r-values required for parameter identification. The identification process and result were presented in this section. Based on the identified models, the predicted yield surface evolution, stress-strain curves, and r-value vs. strain curves were discussed.

Material experiments

Figure 2 shows the testing method and the specimens utilized in the material experiments. The UT tests were performed in various directions from the rolling direction (RD) to transverse direction (TD) at an interval angle of 15°. The deformation data was recorded by digital image correlation (DIC) system. The uniaxial r-value was defined as the ratio of width strain rate $d\varepsilon_w$ to thickness strain rate $d\varepsilon_t$ in the UT tests:

$$r = \mathrm{d}\varepsilon_{\mathrm{w}} / \mathrm{d}\varepsilon_{\mathrm{t}} \tag{37}$$

The procedure of UCTC tests consisted of two parts. Firstly, the uniaxial compression-tension was conducted on the compression-tension (CT) specimen. All the specimens were firstly precompressed to the displacement of -0.52 mm, and then stretched to different amounts of deformation, including to the displacements of 0.76 mm, 1.3 mm, and 1.92 mm, and to rupture, respectively. To prevent the appearance of buckling during the compression process, a small-scale gauge section of the specimen was designed, as seen in Fig. 2. No anti-buckling set-up was used. Secondly, for the unbroken specimens, the cuboid specimen was cut from the deformed gauge section area using wire-cut electrical discharge machining, and further used as the specimen of the uniaxial compression test.

The uniaxial compression tests were conducted along RD for both the as-received sheet and the prestrained sheet experienced the compression-tension deformation. The cuboid specimen with the height of 5 mm was utilized, as seen in Fig. 2. During the uniaxial compression test, the surfaces of the upper and lower dies were mirror polished to minimize the influence of friction.

Figure 3 shows the stress-strain curves of different tests along RD, including the UT, CC, and UCTC tests. The tension stress-strain curve obtained from the CT specimen matched well with that measured from the standard UT specimen, as shown in Fig. 3a. Meanwhile, the stress-strain response of 6061O sheet shows the characteristic of tension-compression symmetry. Table 2 lists the normalized yield stresses and r-values obtained from the UT tests along different directions. Note that the r-values were found to be nearly constant before the appearance of necking on the gauge sections of UT specimens, and therefore the r-values listed in Table 2 were equal to the mean r-values in the range of uniform deformation of the gauge sections.

Figure 3b shows the stress-strain curves of UCTC tests. The compression-tension specimens were firstly compressed to the plastic strain of -2.53%, and then stretched to different strain levels, including to three tensile plastic strains of 1.96%, 5.10%, and 9.73%, and to rupture. The CC tests

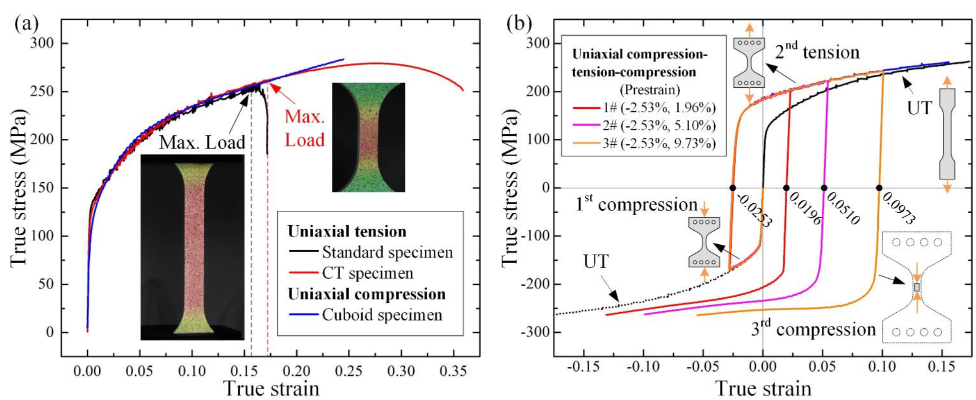

Fig. 3 Stress-strain curves of different tests along RD, (a) uniaxial tension (UT) and uniaxial compression (UC) tests (b) uniaxial compression-tension-compression (UCTC) tests

Table 2 Normalized yield stresses and mean r-values for 6061O sheet

Material	Experimental result							
6061O	σ_0	σ_{15}	σ_{30}	σ_{45}	σ_{60}	σ_{75}	σ_{90}	σ_b
	1	0.9888	0.9694	0.9618	0.9591	0.9632	0.9657	1.0423
	r_0	r_{15}	r_{30}	r_{45}	r_{60}	r_{75}	r_{90}	r_b
	0.6960	0.6223	0.5480	0.4891	0.5548	0.6588	0.7380	1.0139

were further conducted on the cuboid specimens cut from the above unbroken specimens. The stress-strain curves in the final compression loading were offset according to the prestrain in the previous tension loading. Note that the 1st compression stress-strain curves matched well with the curve converted from the UT stress-strain curves, which suggests that the buckling effect could be neglected during the 1st compression process.

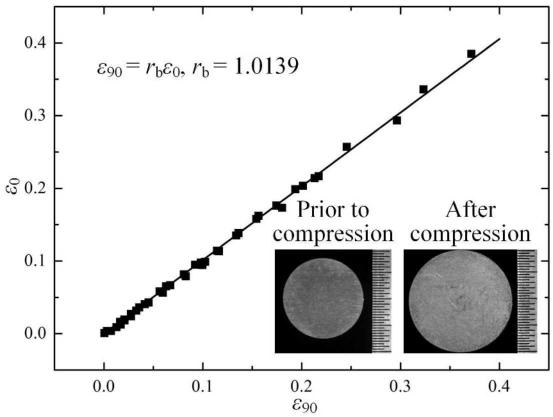

Fig. 4 Strain along RD (ε_0) vs. strain along TD (ε_{90}) under different thickness reduction in the disk compression tests

To identify the parameters in Yld2000-2d function, the though-thickness DC tests were performed using 15 mm diameter disk specimens. The disk specimens were compressed to different amounts of thickness reduction. The normalized yield stress σ_b is list in Table 2. The diameters both parallel to RD and TD of the sheet and the thickness were measured prior to and after the deformation. The variable r_b was defined as:

$$r_b = d\varepsilon_{90}/d\varepsilon_0 \tag{38}$$

where $d\varepsilon_0$ and $d\varepsilon_{90}$ denote the strain rates along RD and TD, respectively. Figure 4 shows the experimental strain along RD (ε_0) vs. strain along TD (ε_{90}) under different thickness reduction. The experimental value of r_b was calculated as

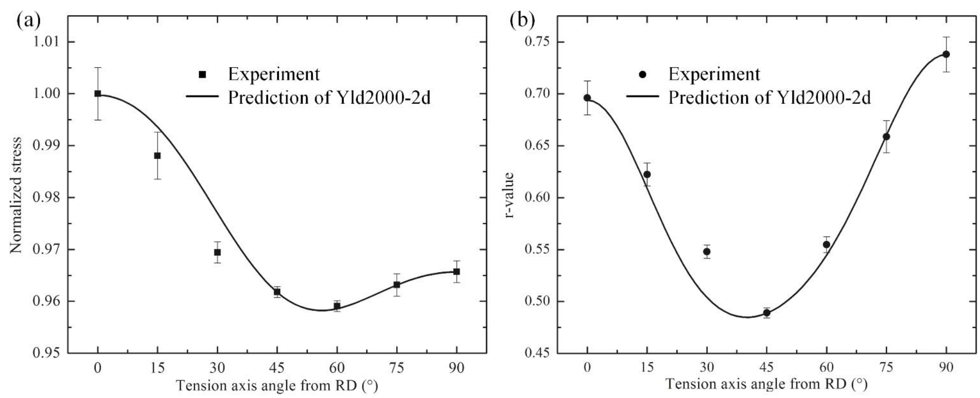

Fig. 5 (a) Tensile yield stresses normalized by RD tensile yield stress, and (b) r-values

Table 3 Identification results of parameters in the yield function and hardening models

Model	Parameter								
Yld2000-2d yield model	m	a_1	a_2	a_3	a_4	a_5	a_6	a_7	a_8
	8	0.9420	0.9998	0.7679	0.9986	1.010	0.9474	0.9195	1.254
Chaboche model	σ_{y0} (MPa)	Q_1 (MPa)	b_1	Q_2 (MPa)	b_2	C_1 (MPa)	γ_1	C_2 (MPa)	γ_2
	125.9	66.2	7.812	56.39	28.43	175.5	35.10	172.3	26.19
	C_3 (MPa)	γ_3							
	97.44	0.01							
enhanced-BRE model	σ_{y0} (MPa)	Q_1 (MPa)	b_1	Q_2 (MPa)	b_2	C_1 (MPa)	γ_1	p_1	q_1
	125.9	17.73	87.18	136.5	11.76	285.6	46.54	-32.37	21.38
	C_2 (MPa)	γ_2	p_2	q_2	C_3 (MPa)	γ_3	p_3	q_3	
	382.7	37.95	38.48	29.86	464.8	31.05	-12.65	44.49	
YU model	σ_{y0} (MPa)	B (MPa)	R_{sat} (MPa)	n	C	b (MPa)	h		
	125.9	151.6	115.5	10.34	59.08	18.80	0.1128		

the slope of linear fit for the relation between ε_0 and ε_{90}, and the value was equal to 1.0139.

Parameter identification

Parameters in yield function

The determination of eight coefficients a_k (k = 1–8) in the Yld2000-2d yield function requires at least eight experimental characteristics. The yield stresses and r-values in UT tests along RD, 45° and TD (i.e. σ_0, σ_{45}, σ_{90}, r_0, r_{45} and r_{90}), as well as the yield stress and r-value in through-thickness DC test (i.e. σ_b and r_b) were employed here. By introducing these values in the yield function and calculation formula of r-value, a set of eight non-linear equations were obtained. The coefficients can thus be determined by solving the equations numerically. Figure 5 shows the experimental normalized yield stresses and r-values, as well as those predicted by Yld2000-2d function using the identified coefficients as listed in Table 3.

Parameters in hardening models

The UT and UCTC stress-strain curves were utilized here to identify the parameters in the three hardening models. For the Chaboche model, a global optimization approach using the non-inferior sorting genetic algorithm NSGA-II was utilized to determine the parameters. For the three back stress components, each of them is defined to individually control a certain segment of the hysteresis curve according to Bari and Hassan [24] and Rahman et al. [25]. Therefore, different segments of the UCTC stress-strain curves were utilized to determine the parameters in different back stress components. Detailed identification process could be referred to the work of Zhang et al. [26]. The final optimal values of the parameters in the Chaboche model are listed in Table 3.

For the YU model, the procedure of parameter identification is introduced in the work of Yoshida and Uemori [8]. The parameters σ_{y0}, B, R_{sat}, n, and b, which have physical meanings, could be determined directly according to the corresponding segments of UT and UCTC stress-strain curves. The rest two parameters C and h were determined through the optimal fitting method using NSGA-II. The minimization of sum of square differences between the experimental and predicted UCTC stress-strain curves was set as the objective of optimization. The result of parameter identification is listed in Table 3.

As for the enhanced-BRE model, the parameters in the Voce + Voce flow stress extrapolation equation were determined using the least square fitting between Eq. (22) and the UT stress-strain curve. As for the parameters in the kinematic hardening, the back stress vs. strain curves of the prestrained sheet are responsible for the identification. In the 1st compression stage of the UCTC experiment, the applied compression stroke was kept small to avoid the buckling effect. This leads to that only one level of the 1st compression strain was obtained (i.e. -0.0253 as seen in Fig. 3). The identification of parameters C_i and γ_i depends on the preloading stage according to Eqs. (15)-(19). Therefore, the result of the 2nd tension tests, which involves only one level of precompression strain, was not suitable for determining the parameters C_i and γ_i alone. As for the 3rd compression tests, multiple prestrain levels were introduced beforehand; meanwhile, the plastic behavior in the 3rd compression stage contains the impact of the former two loading stages. These two features would keep the identification result more reliable. Therefore, the back stress vs. strain curves calculated from the 3rd compression of UCTC tests were utilized to identify the parameters in the kinematic hardening.

In the enhanced-BRE model, the back stress is assumed to stand for the geometrical center from the uniaxial tension stress to the uniaxial compression stress on the yield surface, according to Eq. (23) and Fig. 1b. The back stress is calculated as the half of the difference between the flow stress of the as-received and preloaded sheets in the reference direction. It should be noted that this calculation method is not suitable for other hardening models, such as the Chaboche or YU model, because the definition of back stress is not identical. Figure 6a and b show the equivalent stress-strain curves of UCTC tests and the calculated back stress vs. strain curves, respectively. For the 3rd compression of UCTC tests, the prestrain contains the 1st compression and 2nd tension. In the uniaxial loading condition, the accumulated back stresses at the end of 1st precompression (Point A in Fig. 6a) $\alpha^{\mathrm{A}}_{\mathrm{a}(i)}$ and the 2nd pretension (Point B in Fig. 6a) $\alpha^{\mathrm{B}}_{\mathrm{a}(i)}$ are calculated as:

$$\alpha^{\mathrm{A}}_{\mathrm{a}(i)} = -\frac{C_i}{\gamma_i}\left[1-\exp\left(-\gamma_i\bar{\varepsilon}^{\mathrm{p}}_{\mathrm{A}}\right)\right] \tag{39}$$

$$\alpha^{\mathrm{B}}_{\mathrm{a}(i)} = \frac{C_i}{\gamma_i} + \left(\alpha^{\mathrm{A}}_{\mathrm{a}(i)} - \frac{C_i}{\gamma_i}\right)\exp\left(-\gamma_i\left(\bar{\varepsilon}^{\mathrm{p}}_{\mathrm{B}} - \bar{\varepsilon}^{\mathrm{p}}_{\mathrm{A}}\right)\right) \tag{40}$$

According to Eqs. (39) and (40), the parameters C_i and γ_i were identified through the least squared method by using the values of back stresses once the strain path changes, i.e. at Points A and B in Fig. 6a. During the 3rd compression stage, the active back stress restores from $\alpha^{\mathrm{B}}_{\mathrm{a}(i)}$:

$$\alpha = \sum_{i=1}^{n}\alpha_{(i)} = \sum_{i=1}^{n}\alpha^{\mathrm{B}}_{\mathrm{a}(i)}\left[p_i + (1-p_i)\exp\left(-q_i\left(\bar{\varepsilon}^{\mathrm{p}}_{\mathrm{B}} - \bar{\varepsilon}^{\mathrm{p}}\right)\right)\right] \tag{41}$$

To determine the parameters p_i and q_i, Eq. (41) was utilized to fit the experimental back stress vs. strain curves in the

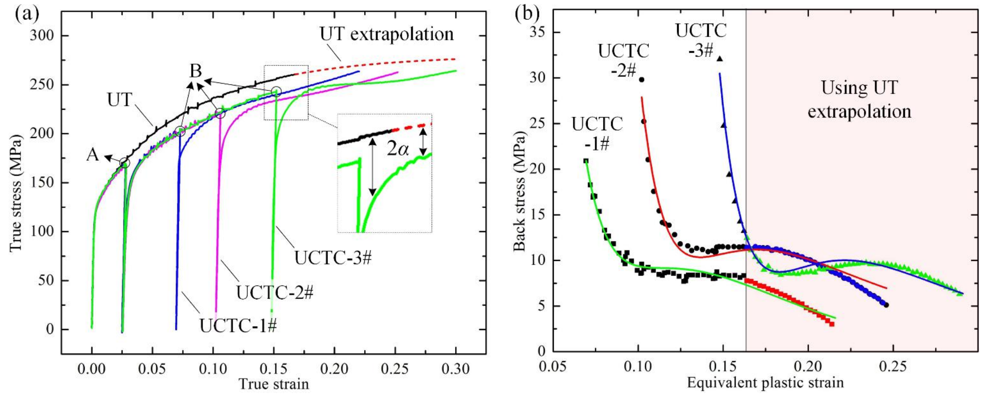

Fig. 6 (a) Equivalent stress-strain curves of UT and UCTC tests (b) Experimental back stress vs. strain curves in the 3rd compression of UCTC tests and those predicted by the enhanced-BRE model

3rd compression of UCTC tests through the least squared method. Fitting result is shown as Fig. 6b, and the values of involved parameters are listed in Table 3.

In summary, the parameters in the enhanced-BRE model can be identified step by step using the experimental results, and the mathematical expressions used for the identification are explicit. Meanwhile, the input value of the back stress is convenient to be obtained. The least squared method which has good convergence ability can be easily applied. By contrast, the isotropic and kinematic hardening components in Chaboche model, as well as the mixed hardening surface for work-hardening stagnation and the mixed hardening bounding surface, are coupled with each other. An iterative optimization method has to be employed for determining the involved parameters. Special attention needs to be paid to the search of the optimal result.

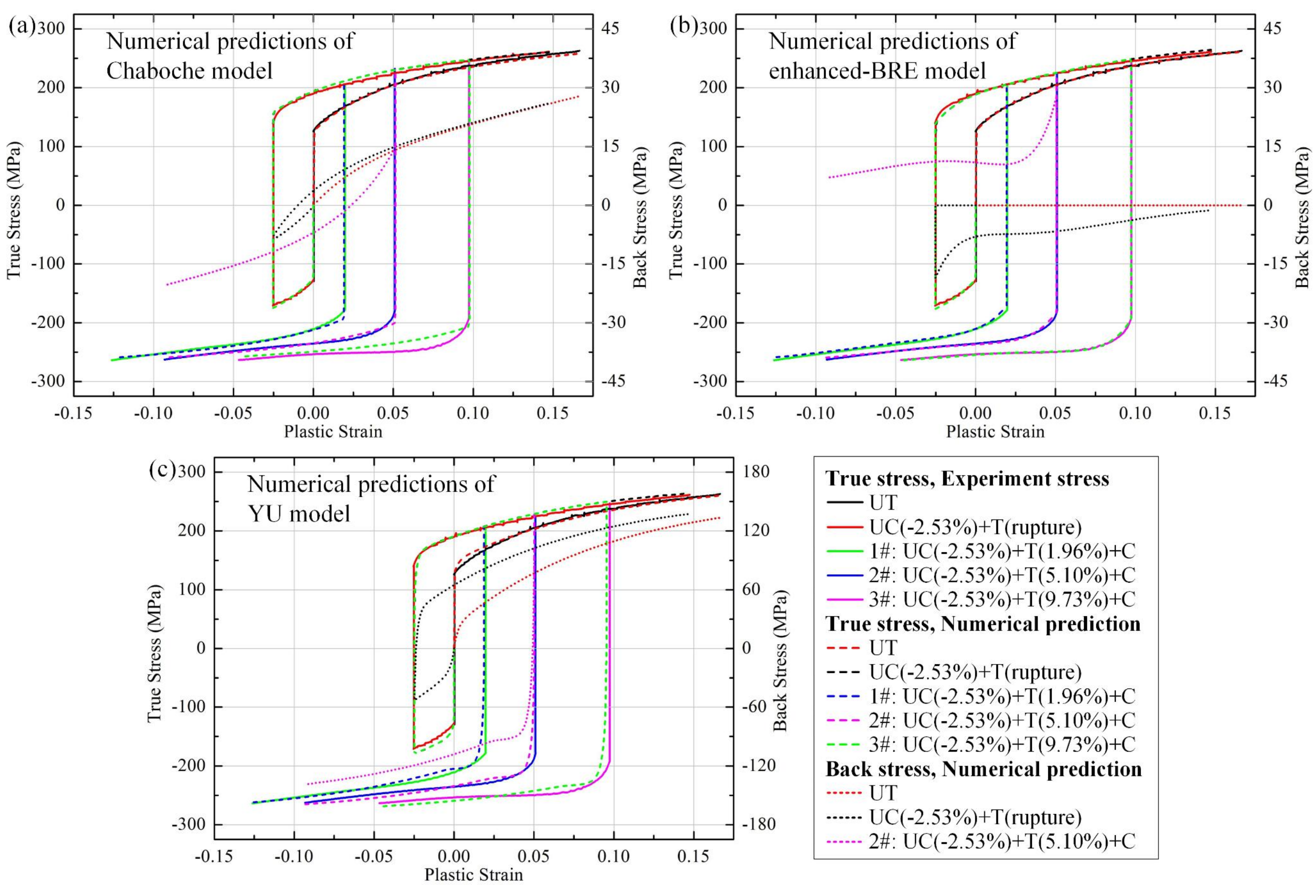

Fig. 7 Stress-strain curves of UT and UCTC tests predicted by different hardening models. (a) Chaboche model, (b) enhanced-BRE model, and (c) YU model

Predicted stress and r-value curves against strain

The stress-strain curves of UT and UCTC tests predicted by different hardening models are compared with the experimental curves, as shown in Fig. 7. Different back stress evolution modes are defined in the models, leading to that the yield surfaces evolve differently as shown in Fig. 8. In Chaboche model, the center of yield surface moves along the current loading direction, and meanwhile the size of yield surface increases as the equivalent plastic strain grows. In contrast, the enhanced-BRE model defines the restoration of back stress, leading to the center of yield surface translates backwards with respect to the current loading direction. The predicted initial yield stress of each subsequent loading stage is lower than that predicted by the Chaboche model, and meanwhile the expansion of yield surface is larger. In YU model, the yield surface moves along the loading direction without expansion. This results in that the initial yield stress in each subsequent loading is quite small.

The three hardening models, which are calibrated by the RD uniaxial tests, were further applied to predict the stress and strain responses along other directions, for instance the TD. Zhang et al. [11] carried out the TD uniaxial tension for the as-received and RD prestretched 6061O sheet. The

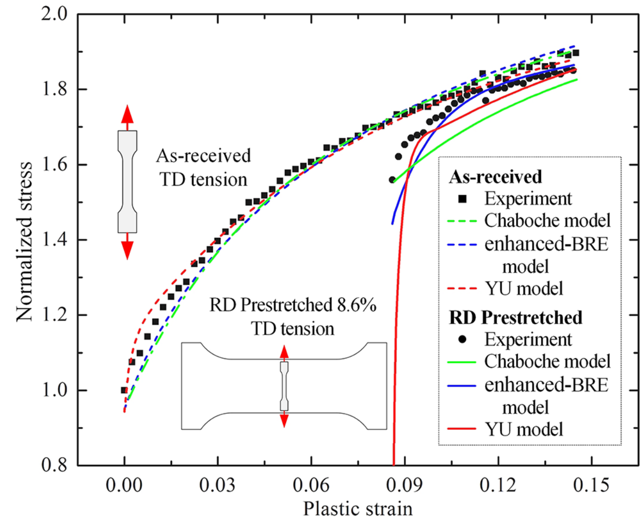

Fig. 9 Normalized TD tension stress-strain curves of the as-received and RD prestretched 6061O sheet predicted by Yld2000-2d yield function and different hardening models

Fig. 8 Yield surface evolution in UCTC tests predicted by Yld2000-2d yield function and different hardening models. (a-c) Chaboche model, (d-f) enhanced-BRE model, and (g-i) YU model

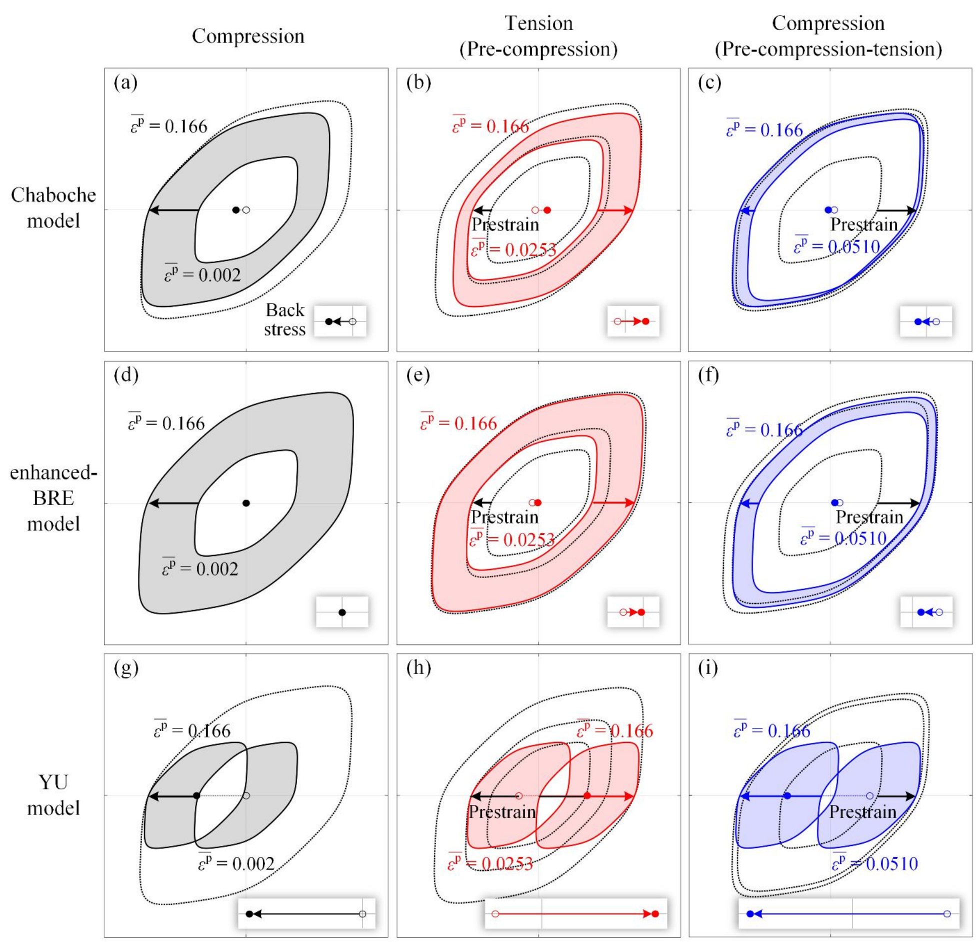

corresponding stress-strain curves normalized by the initial yield stress σ_{y90} are shown in Fig. 9a, as well as the curves predicted by the three hardening models. All the three models could provide a proper prediction result for the TD tension of the as-received sheet. However, for the TD tension stress-strain curve of RD prestretched sheet, the prediction of enhanced-BRE model matched well with the experimental result. In contrast, the initial yield stress predicted by the YU model was very small, and the hardening rate predicted by Chaboche model was lower that the experimental outcome.

The reason that causes the difference between the predicted stress-strain curves lies in the different evolution modes of yield surface controlled by the three hardening models in the RD tension followed by TD tension tests. As seen in Fig. 10, the evolution modes are drawn based on the corresponding simulation result. The solid red and blue arrows denote the stress evolution in the RD pretension and the subsequent TD tension, respectively. Compared with the Chaboche model, the enhanced-BRE model predicted a smaller initial yield stress at the beginning of the subsequent TD tension. As the TD tension strain grew, the back stress recovered gradually, leading to that the yield surface directly moved toward the origin of principle stress coordinate while it expands. As a result, the stress predicted by the enhanced-BRE model increased faster than that predicted by the Chaboche model. The initial yield stress predicted by the YU model in the subsequent TD tension was much smaller, and the back stress grew fast, leading to the rapid increase in the stress-strain curve as depicted in Fig. 9.

If the focus is paid on the comparison between the experimental results and the predictions from the enhanced-BRE model, it can be found that the prediction results are not ideal in small strain level, but become much better at large strains. One reason might be that the distortion of yield surface induced by the preloading was not considered in this work. According to the works of Tozawa [27], Khan et al. [28, 29] and other researchers, the distortion of yield surfaces forming a corner in the front of preloading direction and a flat zone in the rear was observed in metals. In the subsequent loading after preloading, the distortion restored within a small range of strain but never completely recovered. If the distortion of yield surface caused by preloading and its evolution in the subsequent loading was considered, the predicted stresses at small strains would be larger than that predicted here in Fig. 9, which would be closer to the experimental curves. As the deformation grew, the distortion restored gradually, and the effect of distortion was smaller. This explains why the prediction could be close to the experimental result at large strains even if the distortion was not considered.

In addition to the stress-strain relation under variable-path loading conditions, different evolution modes of yield surface controlled by hardening models have a significant influence on the plastic deformation under the associated flow rule. In the abovementioned two-stage loading experiment, the r-values of as-received and RD prestretched sheets in RD and TD tension tests are shown as a function of strain in Fig. 11. For the as-received sheet, the r-values in RD and TD tension tests (r_0 and r_{90}) could be treated as constants as the tensile strain increased. When a RD pretension strain was applied on the sheet, r_0 in the subsequent RD tension remained constant except for small fluctuation, because the strain path was unchanged in this case. By contrast, r_{90} in the subsequent TD tension was large in the beginning of deformation, then decreased rapidly as the tensile strain increased, and finally reached to a saturation value which was larger than its original level.

Numerical predictions of the r-values using the Yld2000-2d yield function and three hardening models are also presented as lines in Fig. 11. For the as-received sheet, r_0 and r_{90} predicted by Chaboche and YU models increased with increasing tensile strain due to the definition of the translation of yield surface. In the enhanced-BRE model only the isotropic expansion of yield surface was taken place in the 1st-stage deformation. Therefore, the r_0 and r_{90} were predicted to be constant, which conforms to the experimental result. As for the RD prestretched sheet, all the three hardening models could predict the downward evolution trend of r_{90} based on the translation and the potential expansion of the yield surface. The YU model defined a large translation of yield surface, which leads to the overestimation of r_{90} at the beginning of and in the process of the subsequent TD tensile deformation. The Chaboche model underestimated the initial value and the decrease rate of r_{90}. The restoration evolution of back stress defined by the enhanced-BRE model enabled the translation of yield surface toward the origin and the expansion of yield surface at the same time, resulting in a rapid decrease rate of r_{90} in the subsequent TD tension. The r-value curves against strain predicted by the enhanced-BRE model had the best match with the experimental curves for both as-received and prestrained sheets.

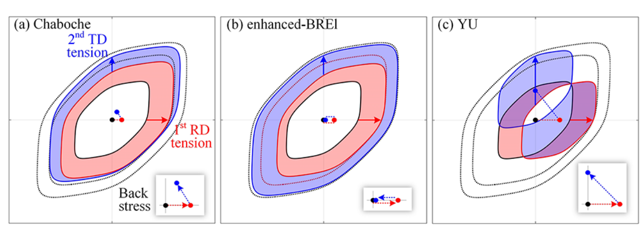

Fig. 10 Yield surface evolution in RD tension-TD tension tests predicted by Yld2000-2d yield function and different hardening models. (a) Chaboche model, (b) enhanced-BRE model, and (c) YU model

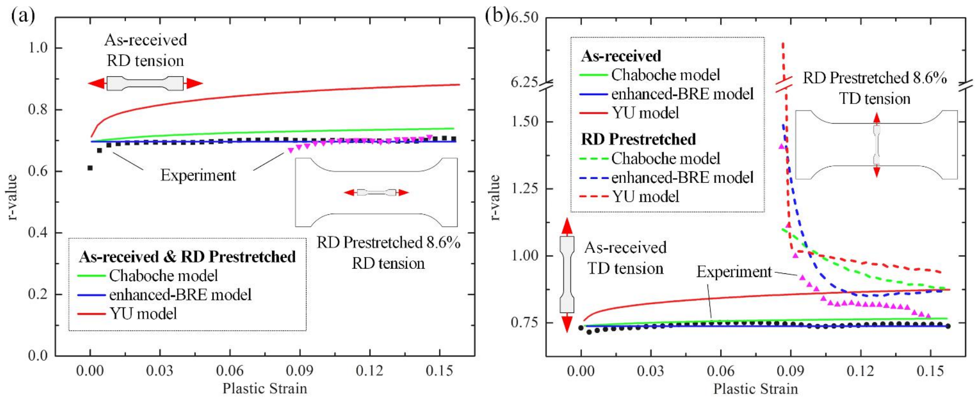

Fig. 11 R-values in RD and TD tension of the as-received 6061O sheet (a) and RD prestretched 6061O sheet (b) predicted by Yld2000-2d yield function and different hardening models

Application in two-stage deep drawing process

To investigate the performance of three hardening models in a practical multi-stage forming process, the two-stage deep drawing of a cylindrical cup was carried out here. Parallel simulation was conducted using the Yld2000-2d yield function and different hardening models. Numerical predicted punch load, geometry of drawn part, and split-ring springbackwere compared with experimental results.

Experimental and numerical modeling

Figure 12a shows the illustration of the two-stage deep drawing process. A circular billet with a diameter of 110 mm cut from the 6061O sheet was drew firstly into a cylindrical cup with the diameter of 85.6 mm and secondly into a cup with the diameter of 63.4 mm. Considering the original thickness of the sheet ($t_0 = 3$ mm), the blank holder was not used. The clearance between the drawing punch and die was set to be $1.1t_0$. The drawing process was carried out on the platform designed by Zhu et al. [30]. The drawing device was fixed at the connecting ends of a universal testing machine, which moved at a speed of 10 mm/min during the experiments. The workpiece was lubricated with zinc stearate. Each drawing stage were repeated at least five times to investigate the reproducibility. The cylindrical cups obtained from each drawing stage were scanned using ATOS-SCAN machine to measure the geometry of the cups. The measurement accuracy is 0.01 mm.

Figure 12b shows the numerical models of the two-stage deep drawing process. The simulation was performed in commercial software ABAQUS/Explicit. One-fourth geometric models were utilized to improve the computation efficiency. Shell elements with four nodes and reduced integration (S4R) were utilized to mesh the one-fourth of the circular blank. The total number of elements was 3414. Five integration points were defined through the thickness. The penalty contact method was adopted and the friction coefficient was set as 0.10. The elastoplastic deformation was assumed for the sheet. Three hardening models, together with Yld2000-2d yield function, were taken to define the plastic response. The models were compiled into VUMAT, by employing a semi-implicit integration using the radial return method to update stress, strain, and other state variables.

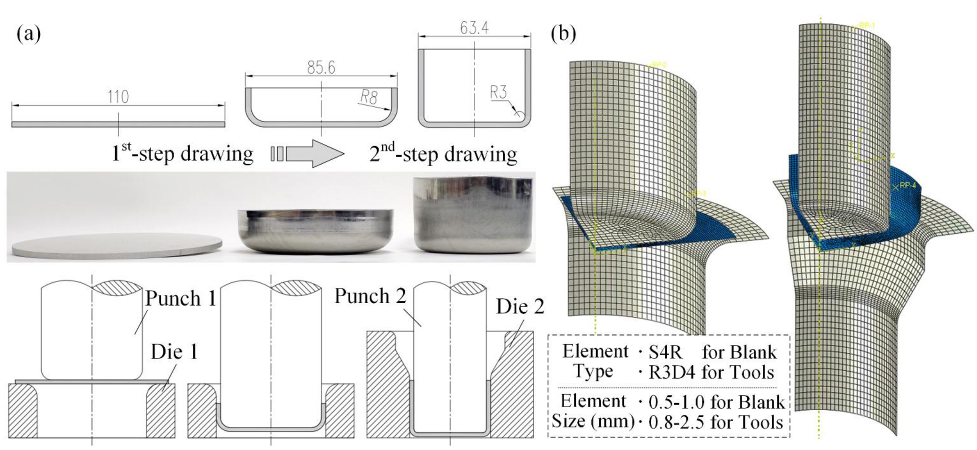

Fig. 12 (a) Cylindrical cups and key tools, and (b) finite element models of the two-stage deep drawing process

Strain path evolution

For the two-stage deep drawing process, local material would experience complex change of strain path. Taking the numerical result predicted by the enhanced-BRE hardening model together with Yld2000-2d yield function as an example, the drawing process is shown in Fig. 13a. Three elements, i.e. E1, E2, and E3, were chosen in the areas contacted with the fillets of two punches and near the outer edge of billet to present the evolution of their strain paths. Since the shell elements with five integration points through thickness were utilized in the simulation, two groups of strain paths corresponding the bottom and top surfaces of the billet were outputted, respectively, as shown in Fig. 13b and c.

At the position of element E1, the bottom surface which was exposed to free air thinned obviously, while the top surface contacting with the two punches had the tendency of thickening. As for the element E2, the evolution of strain path was complex. In the 1st drawing stage, E2 contacted with the fillet of the punch, leading the thinning tendency on the bottom surface and the thickening tendency on the top surface. In the 2nd drawing stage, E2 located at the flange area, and its deformation history could be generally divided into three stages, i.e. the beginning of 2nd drawing A to B, B to C, and C to the end of drawing as seen in Fig. 13b and c. The thickening or thinning tendency of each side of the surface was related to whether the surface was in contact with the tools or not. For example, during the deformation B-C, the bottom surface contacted with the die and showed the tendency of thickening, while the free top surface had the tendency of thinning. The deformation at element E3 always conformed to the circumferential compression according to Fig. 13b and c. It should be noted that in the experimental drawing process, the circumferential compression deformation would lead to an obvious thickening at E3, and after E3 flowed into the clearance of the die and punch, a thinning in thickness happened at the end of each drawing stage. However, because the shell element was utilized in this work, the thinning deformation at E3 could not be simulated.

Punch Load-stroke curves

The experimental punch load as a function of punch stroke in each stage of deep drawing process is presented in Fig. 14. During the each stage of deep drawing process, circumferential contraction was taken place on the flange area firstly. The work hardening resulted in the punch load increasing with the increase of punch stroke. Meanwhile, as the material continued to flow into the cavity of the die, the volume of the material participating in the circumferential contraction decreased gradually, which would lead to the trend that the punch load decreased with the increase of punch stroke. When a balance between these two mechanisms was achieved, the load reached the maximum as shown in Fig. 14. Thereafter, the load decreased with the increase of stroke until the thickened flange material began to flow into the clearance between the punch and die. Simulation result shows that, for the 1st stage the numerical load-stroke curves predicted by three hardening models were close to each other. Obvious difference between the predicted load-stroke curves was found in terms of the peak load of 2nd stage. Among these three hardening models

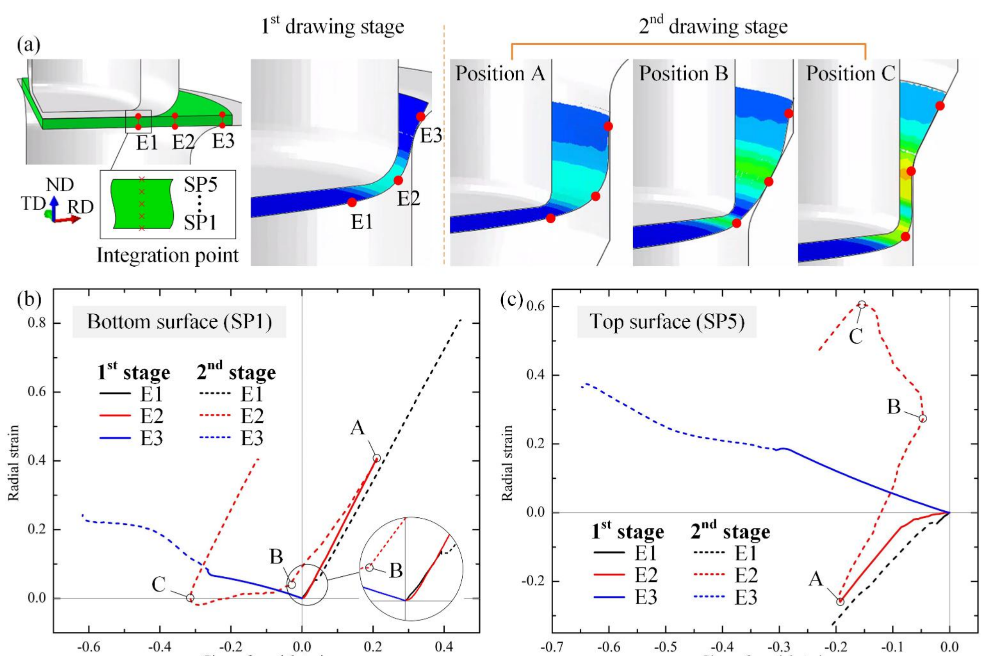

Fig. 13 Numerical result of two-stage deep drawing process (a); the strain path evolution of integration points on the bottom surface (b) and the top surface (c) of the billet

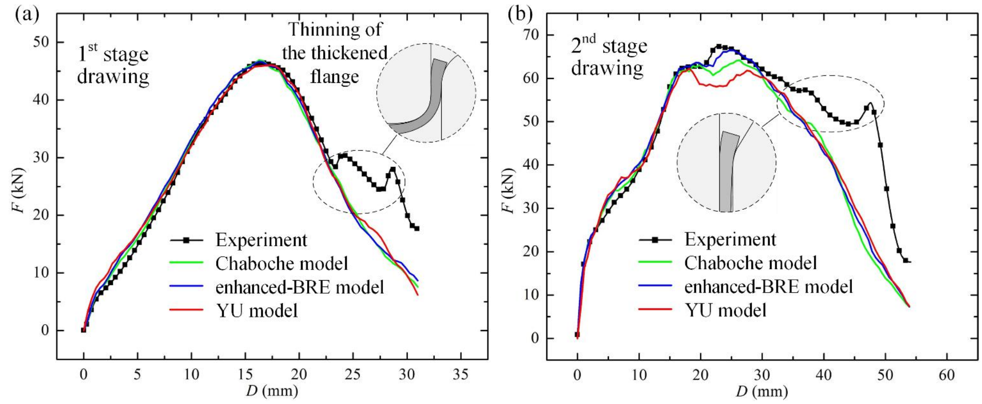

Fig. 14 Experimental load-stroke curves in the two-stage deep drawing process and the numerical ones predicted by Yld2000-2d yield function and different hardening models. (a) 1st stage, and (b) 2nd stage

the enhanced-BRE model has the best prediction accuracy concerning the load-stroke curve. It should be noted that since the shell element, which eliminates the influence of thickness change on numerical calculation, was utilized for meshing the workpiece, the simulation did not reproduce the increase of load caused by the thinning of the thickened flange.

Height distribution and split-ring springback of drawn cup

To compare the prediction accuracy concerning the geometry of the cups, the height distribution of the final cup, as well as the springback when splitting a ring cut from the cup, was utilized. Figure 15a shows the experimental heights measured in Gom Inspect 2016 software, and the numerical heights predicted by the three hardening models associated with Yld2000-2d yield criterion. The thinning of the flange near the end of drawing process, which cannot be reflected by the shell elements, would cause the increase of cup height. Therefore, all the predicted heights were less than the experimental outcome. After the height data was normalized by the height value in RD, the obtained normalized height distribution can denote the earing profile of the drawn cup, which reflects the planar anisotropy in sheet metal. As seen in Fig. 15b, the enhanced-BRE model shew its superiority in predicting the earing phenomenon. Since that the r-value did not remain constant when strain path changes, it can be implied that the proposed hardening model was capable of describing the evolution of r-value during the forming process.

The split-ring test is a convenient method to evaluate the residual circumferential stresses at the sidewall of the deep drawn cups [31]. It consists of the cut of a ring specimen from the cup, the split of the ring, and the measurement the springback caused by the release of residual stresses after splitting. In this work, a 15 mm-height ring was cut at 10 mm from the top of the cup. The ring was then split along the axial direction in RD to allow the opening up, as seen in Fig. 16a. Three repeated experiments were operated and the opening gaps Δs were obtained as bellowing: 4.16 mm, 4.20 mm, and 4.07 mm with the averaged value 4.14 mm. The simulation of split-ring test was realized by using the *Model change option in Abaqus/Standard. The stress release processes caused by the removal of the drawing tools, the cut of the ring, and the split of the ring, were modelled, as seen in Fig. 16b. The comparison of experimental and numerical opening gaps (Δs) is shown as Fig. 17. The gaps of the simulated split-rings with the Chaboche and the enhanced-BRE hardening models were closer to the experimental data comparing with the YU model. The result is compatible with that the Chaboche and enhanced-BRE

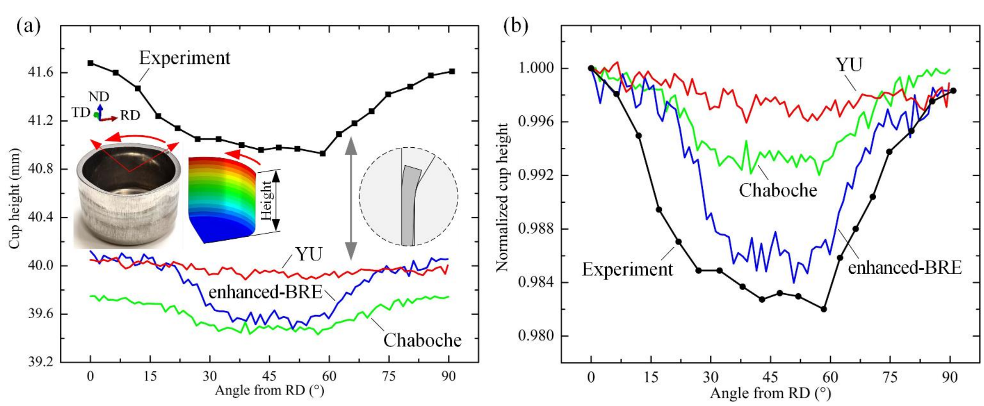

Fig. 15 Comparison of experimental and numerical height distribution of the final cylindrical cup, (a) the real height, and (b) the normalized height

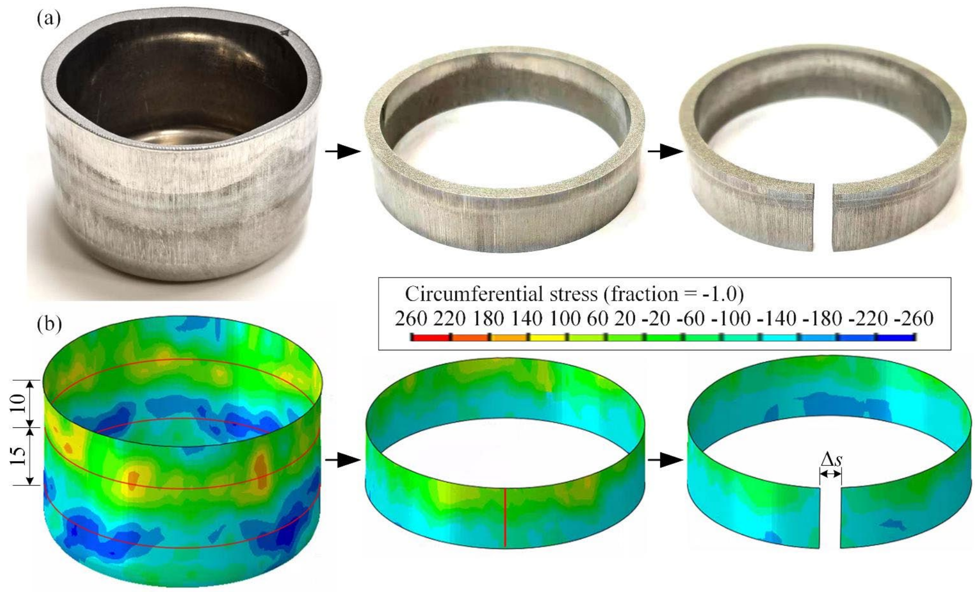

Fig. 16 Process of the split-ring tests (a) Experiment (b) Finite element simulation

models predicted more obvious planar anisotropy distributed in the final cup as seen in Fig. 15b. The planar anisotropy would cause the inconsistent elongation in different radial directions, leading to non-uniform distribution of circumferential stress in the sidewall of drawn cup. Thus a more obvious earing profile predicted by the Chaboche or enhanced-BRE model corresponds to a larger springback in the split-ring simulation.

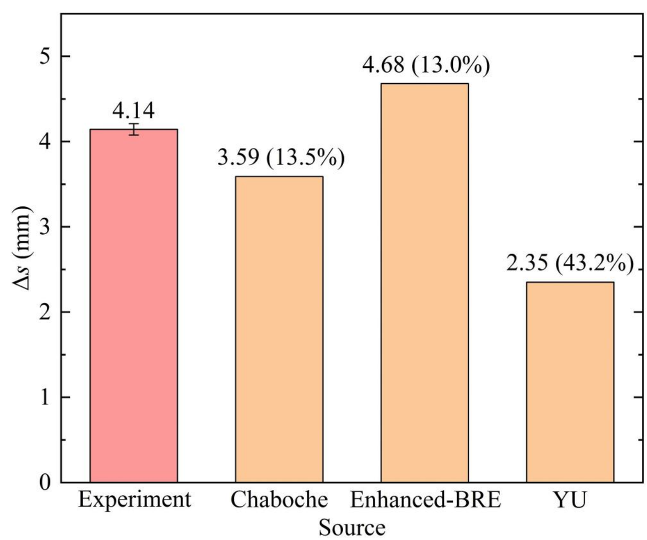

Fig. 17 Comparison of the experimental and numerical opening gaps Δs in the split-ring test (the percentages in brackets after the numerical prediction data represent the relative errors between the numerical and experimental values.)

Conclusions

An enhanced back-stress restoration evolution hardening model was proposed in this work to describe the stress and strain response in strain path change conditions. Comparative study was conducted between the proposed hardening model, Chaboche combined hardening model, and Yoshida-Uemori hardening model, in terms of their predict ability of work-hardening and r-value behavior in reverse and orthogonal loading cases, as well as in a practical two-stage deep drawing process. The following conclusions can be drawn from the analysis:

(1) The predictions of work-hardening and r-value behaviors in orthogonal loading by the proposed hardening model matched well with the experimental results, comparing with Chaboche and Y-U models. Among these three hardening models, the proposed model was preponderant in predicting the early reyielding and permanent softening effect, as well as the r-value transition in the loading conditions beyond those used for parameter identification.

(2) In the two-stage deep drawing process, strain path changed markedly in the second stage. Obvious difference between the prediction results of the three hardening models was observed in this stage, which indicates the significant influence of hardening model on the prediction of plastic response under multi-stage forming process. The predicted punch load-stroke curves and height distribution of drawn parts by the proposed hardening model was closer to the experimental outcome. The springback analysis of the split-ring test shew the good prediction accuracy of the proposed model with respect to the residual stress distribution in the cup formed by the two-stage deep drawing process.

The developed hardening model was validated by the plastic response in the UCTC tests and the RD tension followed by TD tension tests in the current work, and then applied to the two-stage deep drawing process. The applicability to more other loading path change cases, such as tension-shear and shear-reverse shear strain path changes, and practical forming processes remain to be further studied.

Acknowledgements This study was supported by the National Natural Science Foundation of China (51875351) and Shanghai Outstanding Academic Leaders Plan (21XD1422000).

Declarations

Conflict of interest /**Competing Interests**: The authors declare that they have no conflict of interest.

References

1. Peng J, Li K, Dai Q, Peng J (2018) Mechanical properties of pre-strained austenitic stainless steel from the view of energy density. Results Phys 10:187–193. https://doi.org/10.1016/j.rinp.2018.05.034
2. Lee J, Ha J, Bong HJ et al (2016) Evolutionary anisotropy and flow stress in advanced high strength steels under loading path changes. Mater Sci Eng A 672:65–77. https://doi.org/10.1016/j.msea.2016.06.074
3. Ha J, Lee J, Kim JH et al (2017) Investigation of plastic strain rate under strain path changes in dual-phase steel using microstructure-based modeling. Int J Plast 93:89–111. https://doi.org/10.1016/j.ijplas.2017.02.005
4. Hahm JH, Kim KH (2008) Anisotropic work hardening of steel sheets under plane stress. Int J Plast 24:1097–1127. https://doi.org/10.1016/j.ijplas.2007.08.007
5. Prager W (1956) A New method of analyzing stresses and strains in work-hardening plastic solids. J Appl Mech 23:493–496
6. Armstrong PJ, Frederick CO (1966) A mathematical representation of the multiaxial Bauschinger effect. CEGB Report RD/B/N 731. Central Electricity Generating Board, Berkeley
7. Chaboche JL (1986) Time-independent constitutive theories for cyclic plasticity. Int J Plast 2:149–188. https://doi.org/10.1016/0749-6419(86)90010-0
8. Yoshida F, Uemori T (2002) A model of large-strain cyclic plasticity describing the Bauschinger effect and workhardening stagnation. Int J Plast 18:661–686. https://doi.org/10.1016/S0749-6419(01)00050-X
9. Hajbarati H, Zajkani A (2019) A novel analytical model to predict springback of DP780 steel based on modified Yoshida-Uemori two-surface hardening model. Int J Mater Form 12:441–455. https://doi.org/10.1007/s12289-018-1427-2
10. Lin J, Hou Y, Min J et al (2020) Effect of constitutive model on springback prediction of MP980 and AA6022-T4. Int J Mater Form 13:1–13. https://doi.org/10.1007/s12289-018-01468-x
11. Zhang W, Zhuang X, Zhang Y, Zhao Z (2020) An enhanced François distortional yield model: Theoretical framework and experimental validation. Int J Plast 127:102643. https://doi.org/10.1016/j.ijplas.2019.102643
12. Barlat F, Ha J, Grácio JJ et al (2013) Extension of homogeneous anisotropic hardening model to cross-loading with latent effects. Int J Plast 46:130–142. https://doi.org/10.1016/j.ijplas.2012.07.002
13. He J, Gu B, Li Y, Li S (2018) Forming limits under stretch-bending through distortionless and distortional anisotropic hardening. J Manuf Sci Eng 140:121013. https://doi.org/10.1115/1.4041329
14. Lee J, Bong HJ, Kim D, Lee M-G (2020) Modeling differential permanent softening under strain-path changes in sheet metals using a modified distortional hardening model. Int J Plast 133:102789. https://doi.org/10.1016/j.ijplas.2020.102789
15. Qin J, Holmedal B, Zhang K, Hopperstad OS (2017) Modeling strain-path changes in aluminum and steel. Int J Solids Struct 117:123–136. https://doi.org/10.1016/j.ijsolstr.2017.03.032
16. Zaman SB, Barlat F, Kim JH (2018) Deformation-induced anisotropy of uniaxially prestrained steel sheets. Int J Solids Struct 134:20–29. https://doi.org/10.1016/j.ijsolstr.2017.10.029
17. Barlat F, Brem JC, Yoon JW et al (2003) Plane stress yield function for aluminum alloy sheets - Part 1: Theory. Int J Plast 19:1297–1319. https://doi.org/10.1016/S0749-6419(02)00019-0
18. Yang Y, Vincze G, Baudouin C et al (2021) Strain-path dependent hardening models with rigorously identical predictions under monotonic loading. Mech Res Commun 114:103615. https://doi.org/10.1016/j.mechrescom.2020.103615
19. Yang H, Zhang W, Zhuang X, Zhao Z (2020) Calibration of Chaboche Combined Hardening Model for Large Strain Range. Procedia Manufacturing. Procedia Manufacturing, Cottbus, pp. 867–872
20. Nath A, Ray KK, Barai SV (2019) Evaluation of ratcheting behaviour in cyclically stable steels through use of a combined kinematic-isotropic hardening rule and a genetic algorithm optimization technique. Int J Mech Sci 152:138–150. https://doi.org/10.1016/j.ijmecsci.2018.12.047
21. Schmitt JH, Aernoudt E, Baudelet B (1985) Yield loci for polycrystalline metals without texture. Mater Sci Eng 75:13–20. https://doi.org/10.1016/0025-5416(85)90173-9
22. Mánik T, Holmedal B, Hopperstad OS (2015) Strain-path change induced transients in flow stress, work hardening and r-values in aluminum. Int J Plast 69:1–20. https://doi.org/10.1016/j.ijplas.2015.01.004
23. Qin J, Holmedal B, Hopperstad OS (2019) Experimental characterization and modeling of aluminum alloy AA3103 for complex single and double strain-path changes. Int J Plast 112:158–171. https://doi.org/10.1016/j.ijplas.2018.08.011
24. Bari S, Hassan T (2000) Anatomy of coupled constitutive models for ratcheting simulation. Int J Plast 16:381–409. https://doi.org/10.1016/S0749-6419(99)00059-5
25. Rahman SM, Hassan T, Ranjithan SR (2005) Automated parameter determination of advanced constitutive models. In: Proceedings of PVP2005: 2005 ASME Pressure Vessels and Piping Division Conference. pp 1–12
26. Zhang W, Yang H, Zhuang X et al (2020) Crack initiation prediction eliminating the influence of loading path change: Prediction strategy and model validation. Int J Mech Sci 183:105791. https://doi.org/10.1016/j.ijmecsci.2020.105791
27. Tozawa Y (1978) Plastic deformation behavior under conditions of combined stress. In: Koistinen, D.P., Wang, NM. (eds) Mechanics of Sheet Metal Forming. Springer, pp 81–110
28. Khan AS, Kazmi R, Pandey A, Stoughton T (2009) Evolution of subsequent yield surfaces and elastic constants with finite plastic deformation. Part-I: A very low work hardening aluminum alloy (Al6061-T6511). Int J Plast 25:1611–1625. https://doi.org/10.1016/j.ijplas.2008.07.003
29. Khan AS, Pandey A, Stoughton T (2010) Evolution of subsequent yield surfaces and elastic constants with finite plastic deformation. Part II: A very high work hardening aluminum alloy (annealed 1100 Al). Int J Plast 26:1421–1431. https://doi.org/10.1016/j.ijplas.2009.07.008
30. Zhu S, Zhuang X, Xu D et al (2019) Flange forming at an arbitrary tube location through upsetting with a controllable

deformation zone. J Mater Process Technol 273:116230. https://doi.org/10.1016/j.jmatprotec.2019.05.011

31. Simões VM, Oliveira MC, Neto DM et al (2018) Numerical study of springback using the split-ring test: influence of the clearance between the die and the punch. Int J Mater Form 11:325–337. https://doi.org/10.1007/s12289-017-1351-x